ASME Journal of Heat and Mass Transfer
Online journal at:
https://asmedigitalcollection.asme.org/heattransfer

Thermal Performance of Triply Periodic Minimal Surface Lattice Structures in Single-Phase Dielectric Fluid Cooling of Power Electronics

U. Kemerli[1]
George W. Woodruff School of Mechanical Engineering,
Georgia Institute of Technology,
Atlanta, GA 30332
e-mail: ubade.kemerli@me.gatech.edu

G. Moreno
Advanced Power Electronics and Electric Machines Group,
National Renewable Energy Laboratory,
Golden, CO 80401

R. Chaudhary
Advanced Power Electronics and Electric Machines Group,
National Renewable Energy Laboratory,
Golden, CO 80401

S. Narumanchi
Advanced Power Electronics and Electric Machines Group,
National Renewable Energy Laboratory,
Golden, CO 80401

Y. Joshi
George W. Woodruff School of Mechanical Engineering,
Georgia Institute of Technology,
Atlanta, GA 30332

Additive manufacturing has transformed thermal management by enabling the production of complex, optimized geometries that conventional manufacturing methods cannot achieve. This study investigates the single-phase convective heat transfer performance of gyroid triply periodic minimal surface (TPMS) lattice structures with functional porosity. TPMS structures provide high surface area to volume ratios and are amenable to 3D printing. A gyroid numerical model was created and validated against an existing experimental study with a similar feature size to the investigated geometries. The TPMS structure has a periodic width of 1.6 mm, a length of 10 mm, and a height of 4 mm, with a functional porosity ranging from 0.5 to 0.8, decreasing with distance from the heated surface. Three different flow configurations were examined for an inlet fluid temperature of 70 °C. The inlet velocities range from 0.01 to 1.2 m/s, corresponding to a Reynolds number range of 10–900 with a heat flux of 50 W/cm^2 applied at the base. AmpCool® AC-110 dielectric fluid (Prandtl number 59.5) was used as the coolant. Thermal performance and friction characteristics were studied for the three flow orientations. The parallel flow configuration was identified as the most efficient for heat removal. A detailed analysis of the numerical results highlights the underlying physics behind the thermal performance differences among the flow configurations. [DOI: 10.1115/1.4069386]

Keywords: triply periodic minimal surface (TPMS), power electronics, cooling, thermal management

1 Introduction

Rapid advancements in electric-drive vehicles (EDVs), driven by the introduction of wide-bandgap devices such as silicon carbide, have increased the need for effective thermal management solutions in EDV power electronics to ensure optimal performance, safety, and reliability. Silicon carbide devices generally have a smaller footprint than silicon devices, resulting in higher heat fluxes [1,2]. Various high-heat-flux cooling techniques, such as microchannel cooling [3], spray cooling [4], and jet impingement cooling [5], are available for power electronics devices. Due to its design simplicity and high reliability, single-phase forced convection liquid cooling remains the preferred method for high-power-density power electronics [6]. Additionally, novel heat sink geometries, such as metal foams [7] and triply periodic minimal surface (TPMS) lattice structures [8], have gained significant attention in recent years due to their potential to enhance heat transfer and reduce overall thermal resistance.

Ansari and Duwig [9] investigated a gyroid-based TPMS heat sink for electronic cooling. Through simulations and experimental validation, they demonstrated its superior thermal performance compared to traditional designs. Wei et al. [10] reported that TPMS-based radiators exhibit lower overall average temperatures and enhanced heat dissipation compared to conventional square-structure radiators. Khalil et al. [11] studied the forced convective heat transfer of TPMS heat sinks and reported that they generally induce a highly tortuous spiral flow. Additionally, a recent review by Yeranee and Rao [12] examined flow and heat transfer enhancement in cooling channels incorporating TPMS structures. Chen et al. [13] experimentally investigated gyroid-type TPMS heat sinks and reported a thermal resistance decrease by around a factor of 2.4 compared to pin-fin heat sinks. Hajialibabaei and Saghir [14] experimentally studied three Fischer–Koch-S type TPMS heat sinks with uniform porosities, and one with graded porosity along the flow direction. The 0.6 porosity TPMS heat sink showed the best performance, reaching 0.23 °C/W at 0.019 kg/s. Graded TPMS designs have also been investigated for heat exchangers. Oh et al. [15] studied graded TPMS heat exchangers and achieved 30% enhancement in heat transfer and 28% improvement in thermal performance factor.

The current state of the art in EDV cooling uses a water–ethylene glycol (WEG) coolant in single-phase conditions. Dielectric fluids present a superior approach to reducing thermal resistance between

[1]Corresponding author.

Contributed by the Heat Transfer Division of ASME for publication in the Journal of Heat and Mass Transfer. Manuscript received May 15, 2025; final manuscript received July 31, 2025; published online September 15, 2025. Assoc. Editor: Vijay K. Dhir.

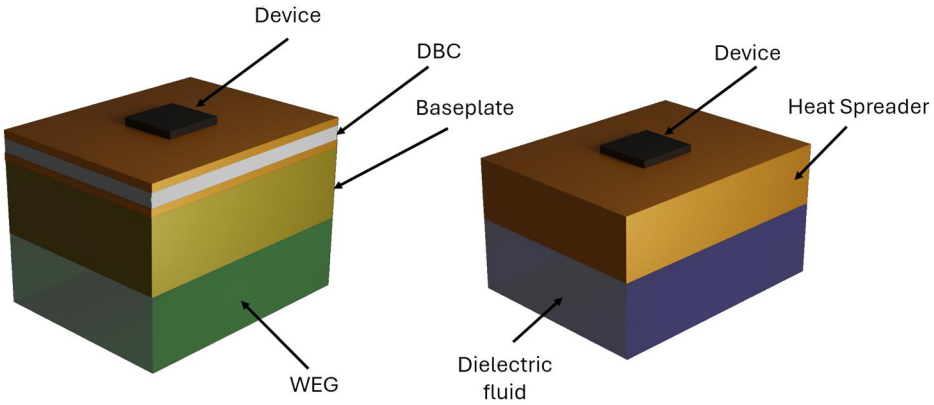

Fig. 1 Three-Dimensional illustration of the conventional power module (left) and low-thermal-resistance packaging (right) for dielectric fluid use (DBC: direct-bond copper)

the electronic device junction and the coolant by eliminating ceramic substrate layers and allowing for direct contact between the coolant and the active device, as illustrated in Fig. 1. Bar-Cohen [16] documented the use of dielectric fluids for cooling electronics. These fluids have been used with pool [17] or flow boiling [18], although some studies have investigated single-phase forced convection. Kelly et al. [19] presented a comparison study for different dielectric fluids for forced convection cooling of power electronics. Sung and Mudawar [20] used HFE 7100 to cool high power density devices with a hybrid cooling scheme combining microchannel and impingement jet, and achieved a cooling performance of 304.9 W/cm^2. Muslu et al. [21] used OptiCool-A with an integrated cooling approach and reported up to 27% increase in maximum heat flux capability compared to the standard packaging approach. Mendizabal et al. [22] studied Novec 7300 for direct cooling of a planar magnetic converter and achieved an 80% lower thermal resistance (0.1 °C/W versus 0.49 °C/W) with an estimated 80% reduction in pressure drop (2 kPa versus 10 kPa) compared to a cold plate benchmark. Moreno et al. [23] predicted that their direct cooling concept achieved a 56% reduction in junction-to-fluid thermal resistance compared to WEG-based cooling systems.

Expanding upon direct cooling concepts, this study investigates the use of TPMS structures as a direct attached heat spreader with graded porosity, with different coolant flow orientations. Dielectric coolant is utilized under single-phase flow conditions, contrary to most TPMS studies that used WEG mixture as the coolant. In addition, using dielectric fluids limits the maximum heat transfer capabilities and power density levels due to their poor properties compared with water-based coolants [24], requiring advanced heat transfer geometries having a high surface area to volume ratio. Also, the effects of graded porosity and its impact on thermal performance remain largely unexplored in the existing literature.

This study aims to reveal the effects of different orientations of graded porous TPMS used with dielectric coolant. The main objective of this study is to propose a preferred orientation and reveal the effects of graded porosity on improved thermal performance.

2 Method

The methodology of this study involved defining the geometries, setting up the numerical model, determining the nondimensional parameters for performance characterization, conducting a mesh dependency analysis, and finally validating the numerical model with experimental data. The study summarizes interesting findings toward using TPMS structures as direct-attach heat spreaders in power electronics.

2.1 Geometries. This study investigates the gyroid TPMS structures formed by surfaces derived from implicit functions. The surfaces are generated using the level-set approximation equation for gyroid [25]

$$\sin(X)\cos(Y) + \sin(Y)\cos(Z) + \sin(Z)\cos(X) = c \qquad (1)$$

The periodicity is represented as $X = 2\pi n_x x$, $Y = 2\pi n_y y$, and $Z = 2\pi n_z z$ in each Cartesian coordinate. Therefore, n_x, n_y, and n_z define the unit cell dimensions.

The parameter c on the right-hand side of Eq. (1) is the level-set constant, and it controls the gyroid minimal surface. The solid structure is formed by solidifying the volume enclosed by a specific c value. Therefore, adjusting c alters the porosity of the generated TPMS lattice structure. TPMS lattices with varying porosities are shown in Fig. 2.

The functional graded TPMS is assumed to be used in a half-bridge inverter, as shown in Fig. 3. The gyroids have dimensions of 10 mm × 10 mm and a height of 4 mm. To reduce computational cost, the flow domain is selected with a width of 1.8 mm, corresponding to the unit cell length, as the geometry exhibits periodicity with this dimension.

Three different flow configurations were investigated in this study, all derived from a gyroid TPMS structure featuring a porosity of 0.5 at the bottom (closer to the heat source) and 0.8 at the top, resulting in a volume average porosity of 0.65.

The flow orientation differs for each model:

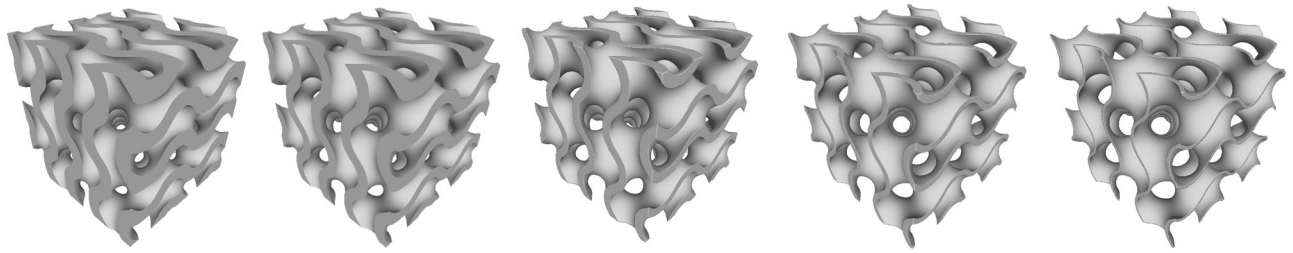

Fig. 2 TPMS lattices with different porosities (0.5, 0.6, 0.7, 0.8, and 0.9)

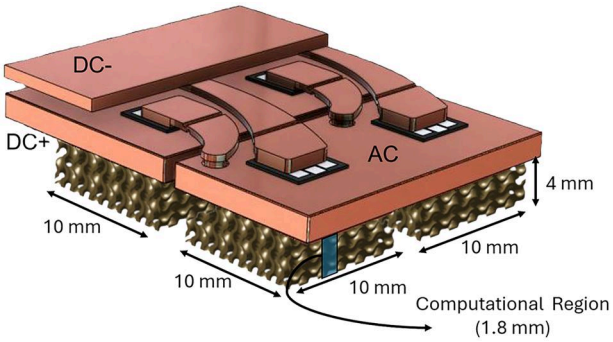

Fig. 3 Conceptual half-bridge module for the use of dielectric fluid and TPMS structure

- Wide slot configuration (Fig. 4(*a*)): This model has a slot jet width of 9 mm. The flow enters from above and exits from the sides.
- Narrow slot configuration (Fig. 4(*b*)): This model has a slot jet width of 2 mm, with an opening in the flow path at the center. As a result, the flow directly impinges on the heated surface. The flow then exits from the sides like the previous model.
- Parallel flow configuration (Fig. 4(*c*)): This model features a parallel flow configuration, where the fluid enters from one side and flows through the structure.

2.2 Numerical Model. Simulations were performed by ANSYS FLUENT 2024 R2 to solve the continuity, momentum, and energy equations. The laminar flow model was utilized because the feature sizes are too small, and the maximum Reynolds number (Re) based on height and TPMS feature sizes are 110 and 830, respectively. The governing equations are [26,27]

$$\nabla \cdot \rho \mathbf{V} = 0 \tag{2}$$

$$\nabla \cdot \rho \mathbf{V}\mathbf{V} = -\nabla p + \nabla \tau \tag{3}$$

$$\nabla \cdot (\rho c_p \mathbf{V} T) = k \nabla^2 T \tag{4}$$

In Eqs. (2)–(4), ρ is the density (kg/m^3), $\mathbf{V}$ is the velocity vector (m/s), p is pressure (N/m^2), τ is the stress tensor (units of tensor components, N/m^2), c_p is specific heat (J/kg K), and T is temperature (K). The energy equation for the solid phase is given by

$$k_s \nabla^2 T = 0 \tag{5}$$

In Eq. (5), k_s is the thermal conductivity of solid (W/m K). A no-slip boundary condition for fluid flow and coupled boundary condition for heat transfer are used at fluid–solid interfaces. Coupled heat transfer boundary condition ensures continuity of temperature (i.e., $T_f = T_s$) and heat fluxes ($-k_f(\partial T_f/\partial n) = -k_s(\partial T_s/\partial n)$) at the fluid–solid interfaces. Inlet and outlet boundary conditions are shown with arrows in Fig. 4. Velocity inlet and pressure outlet boundary conditions are used. The inlet temperature is set to 70 °C, a typical value for EDV power electronics WEG based coolant inlet temperature. All the other sides are defined as adiabatic walls. A heat flux of 50 W/cm^2 is applied at the bottom of the heat spreader. Symmetry boundary conditions are imposed on the sides of the unit cell model. The solid was selected as copper, with a density and thermal conductivity of 8978 kg/m^3 and 387.6 W/m K, respectively. The semi-implicit method for pressure-linked equations scheme has been used for pressure–velocity coupling with second-order upwind discretization for convective terms of momentum and energy equations. The pressure is interpolated at faces using a second-order scheme from cell centers. Other terms, such as diffusion and viscous stresses, are discretized using a second-order central differencing scheme. The gradients, as needed, are estimated using a least-squares cell-based approach in ANSYS-FLUENT. The scaled (scaled based on the first five iteration residuals) convergence criteria were set to 10^{-3} for continuity and momentum equations, and 10^{-7} for the energy equations.

Table 1 AmpCool® AC-110 properties

Property	Value	SI unit
Density	783	kg/m^3
Specific heat	2326	J/kg K
Thermal conductivity	0.134	W/m K
Viscosity	0.0034	kg/m s
Dielectric constant	2.08	N/A

Dielectric fluids offer a promising alternative by enabling direct contact cooling of heated surfaces by eliminating ceramic materials without the risk of electrical short circuits, thus reducing thermal resistance. AmpCool® AC-110 is a dielectric fluid intended for EDVs. It combines key features such as high dielectric strength, thermal stability, and low viscosity. While its thermal conductivity is lower than that of water-based coolants, its electrical insulation allows placement much closer to the heat source, partially compensating for the difference. The properties of AmpCool AC-110 used in the simulations, as shown in Table 1, were obtained from the datasheet [28] and interpolated for 70 °C.

The study covers a range of inlet velocities, volumetric flow rates, and Re, as summarized in Table 2. The flow is assumed to be laminar and incompressible.

2.3 Data Reduction. The gyroid structures occupy a $10 \times 10 \times 4$ mm volume on the cold plate surface. To reduce computation time, a smaller computational domain of 1.8 mm × 10 mm with a height of 4 mm was used as the unit cell model. Additionally, the heat spreader has a thickness of 0.4 mm.

Re is calculated by

$$\mathrm{Re} = \frac{\rho V H}{\mu} \tag{6}$$

where μ is the viscosity of the fluid, V is the superficial average velocity parallel to the heated surface, and H is the channel height, which is assumed to be 4 mm in this study.

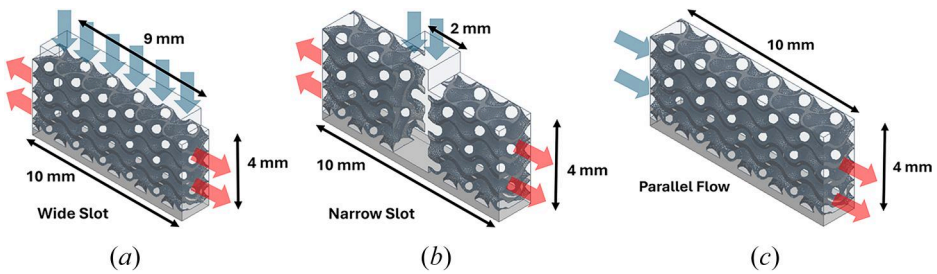

Fig. 4 Different flow orientations/configurations

Table 2 Numerical parameter ranges

Parameter	Range	SI unit
Inlet velocity	0.01–1.2	m/s
Volumetric flow rate	1.6×10^{-7}–6.5×10^{-6}	m^3/s
Volumetric flow rate	0.01–0.4	L/min
Re based on height	10–850	N/A
Re based on the hydraulic diameter of the channel	15–600	N/A

h is calculated as

$$h = \frac{T_s - T_{\text{in}}}{q} \tag{7}$$

where T_s is the heated surface temperature (°C), T_{in} is the fluid inlet temperature (°C), and q represents the heat flux applied to the heat spreader surface (W/m^2).

Nusselt number (Nu) is determined using the channel height as the characteristic length

$$\text{Nu} = \frac{hH}{k} \tag{8}$$

where k is the thermal conductivity of the fluid.

Pumping power (W) is calculated from the following equation:

$$\text{PP} = \dot{V}\Delta P \tag{9}$$

where $\dot{V}$ is the volumetric flow rate (m^3/s), and ΔP is the pressure difference between the inlet and outlet (N/m^2).

2.4 Numerical Uncertainty. A grid independence study is performed for all configurations. The mesh is first generated in tetrahedral control volumes. Next, it is converted into polyhedral control volumes to enhance the numerical accuracy and convergence at a lower computational cost. The numerical uncertainty was estimated by the calculation of the relative difference between the selected mesh and a finer mesh for each flow configuration. The numerical uncertainty was quantified using the following expression:

$$\text{Numerical uncertainty}\,(\%) = \left|\frac{\text{Ø}_{\text{selected}} - \text{Ø}_{\text{fine}}}{\text{Ø}_{\text{fine}}}\right| \times 100 \tag{10}$$

where $\text{Ø}_{\text{selected}}$ and Ø_{fine} are the quantities of interest (either heat transfer coefficient or pumping power) obtained from the selected and finer meshes, respectively.

Table 3 presents the heat transfer coefficients and pumping power values, estimated based on Eqs. (7) and (9). For all three configurations, the relative errors in both heat transfer coefficient and pumping power were found to be less than 1%, with values typically in the range of 0.1% to 0.6%. These small differences confirm that the selected meshes lie within the asymptotic range of mesh convergence and that the numerical results are effectively mesh-independent.

2.5 Model Validation. Using a mesh element size identical to that obtained in the grid independence study, the numerical model is validated against the experimental results of Deng et al. [29], as their study presents a geometry most comparable to the TPMS, with feature sizes around 500 μm. The model used for the validation is shown in Fig. 5, and the comparison between the experimental data and numerical results is presented in Fig. 6, demonstrating reasonable agreement with maximum and average deviation of 9.1% and 7.2%, respectively. However, the numerical Nu is slightly higher, likely because the numerical model does not capture all thermal resistances present in the experimental setup, and the shorter entrance length in the simulations may lead to an underdeveloped flow and thus higher heat transfer.

3 Results and Discussion

The comparative heat transfer results with the variation of Re for different geometries and flow orientations are presented in Fig. 7. The narrow slot configuration exhibits a higher Nu compared to the wide slot, as direct impingement onto the heated surface enhances heat transfer. Interestingly, despite the absence of impingement, the parallel flow configuration achieves a comparable Nu to the narrow slot configuration and surpasses it at higher Re. It can also be noted that, in terms of flow orientation, the narrow slot can be considered as the combination of parallel flow and wide slot. Therefore, it results in between these two in the heat transfer results.

Evaluating Nu across different Re conditions helps understand the hydrodynamic effects on heat transfer. However, analyzing Nu at a fixed pumping power is also crucial, as shown in Fig. 8. The results indicate that all three configurations exhibit similar Nu trends with increasing pumping power. However, the parallel flow configuration slightly outperforms the narrow slot and wide slot configurations with increases of 8.2% and 10%, respectively, under higher pumping power conditions. This highlights that the higher pumping power pushes fluid efficiently through the case with the most resistive flow path, which then results in better performance. At lower pumping power or lower flow rates, the least resistive case is preferred, i.e., narrow slot cases perform better.

The streamlines in the wide slot configuration are shown in Fig. 9 for the highest inlet velocity (0.4 m/s). The fluid enters from a 9 mm slot. However, for simplicity, the streamlines are tracked at three locations (via a 1-mm-wide plane) on the fluid inlet surface. Figure 9(*a*) illustrates the flow distribution within the TPMS geometry, where no direct impingement occurs, preventing the flow from directly reaching the heated surface. Instead, the flow is directed toward the outlet section near the heated surface. The flow farther from the center, shown in Fig. 9(*b*), exits through the upper regions, unable to reach the heated surface effectively. Similarly, the flow near the edges, shown in Fig. 9(*c*), is guided toward the outlet through upper regions, where the heat transfer rate per unit pressure drop is lower due to reduced solid temperatures.

Streamlines for the narrow slot configuration are shown in Fig. 10 for the highest inlet velocity (1.2 m/s). The flow originating from a 1-mm thickness in the center of the 2-mm slot, shown in Fig. 10(*a*),

Table 3 Grid independence and numerical uncertainty

Wide slot					Narrow slot					Parallel flow				
Mesh element (M)	h (W/m^2 K)	Difference %	P_{pump} (W) $\times 10^4$	Difference %	Mesh element (M)	h (W/m^2 K)	Difference %	P_{pump} (W) $\times 10^3$	Difference %	Mesh element (M)	h (W/m^2 K)	Difference %	P_{pump} (W) $\times 10^3$	Difference %
1.14	21,810	10.9	6.0122	1.2	1.00	29,528	2.6	2.6974	0.8	1.08	32,654	3.6	3.4165	0.5
2.63	21,648	10.1	6.0250	1.1	2.36	29,301	1.8	2.6965	0.8	2.5	32,613	3.4	3.4240	0.3
6.31	19,556	0.6	6.0755	0.2	5.30	28,618	0.6	2.7166	0.1	5.78	31,619	0.3	3.4292	0.1
8.55	19,666	—	6.0896	—	7.16	28,776	—	2.7195	—	7.56	31,533	—	3.4336	—

Note: The shaded row indicates the selected mesh.

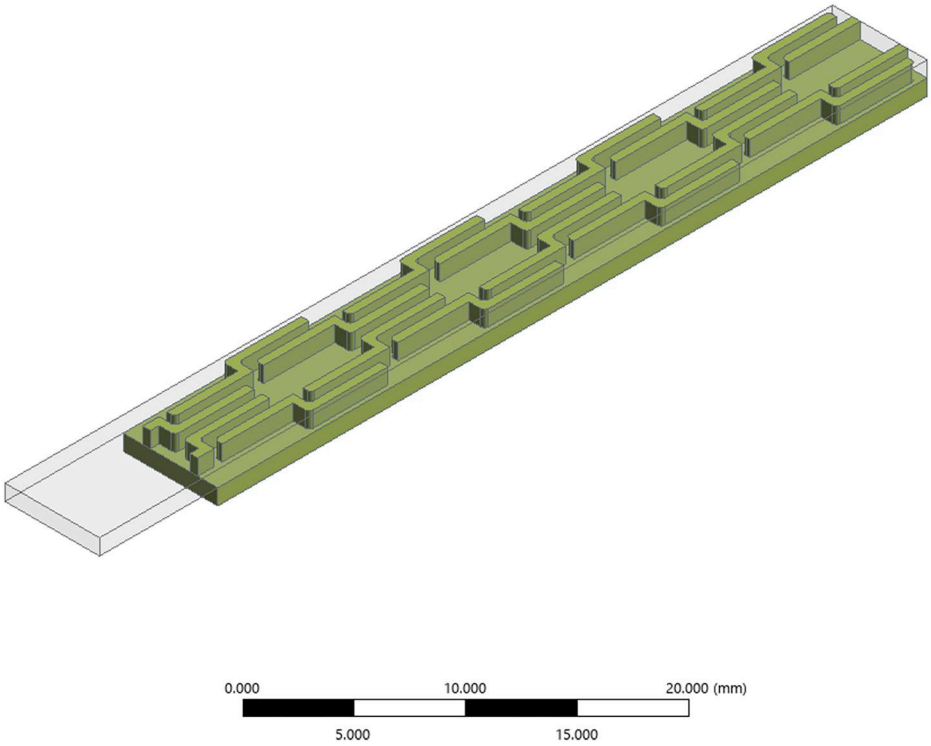

Fig. 5 Validation model

travels directly to the heated surface, where it is distributed throughout the TPMS geometry and exits on both sides. In contrast, the flow originating from the 0.5-mm section near the edge, illustrated in Fig. 10(*b*), enters into the TPMS geometry and exits primarily from the upper regions of the outlet. In general, this configuration generates more vorticity compared to the wide slot configuration.

The streamlines for the parallel configuration are shown in Fig. 11 for the highest inlet velocity (0.4 m/s). Figure 11(*a*) shows the streamlines originating from the upper part of the inlet section, and Fig. 11(*b*) shows the streamlines originating from the lower part of the inlet section. The fluid entering the lower part of the inlet is predicted to spread upward more than the downward spreading from the upper part of the inlet. This is due to the increased porosity and associated lower flow resistance in the upper region.

The following results show the vorticity magnitude in the flow field for different cases. It is defined as follows:

$$|\boldsymbol{\omega}| = \sqrt{\omega_x^2 + \omega_y^2 + \omega_z^2} \tag{11}$$

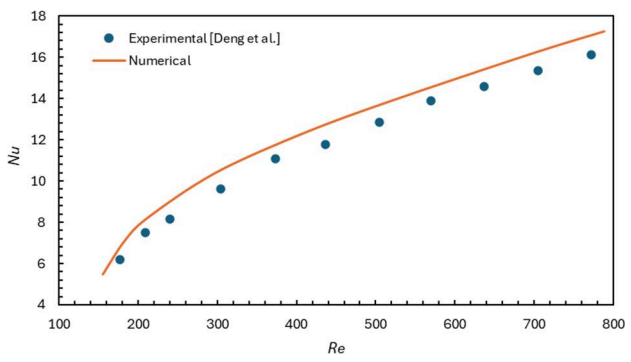

Fig. 6 Agreement between experimental and numerical results

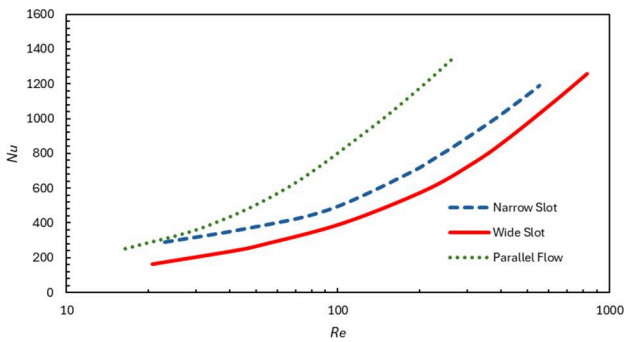

Fig. 7 Nu with varying Re for different configurations

The vorticity results for the wide slot geometry are shown in Fig. 12. The central region generates minimal vorticity. This indicates that directing flow from upwards creates a weak flow mixing at the central regions, resulting in a weaker heat transfer performance. In contrast, vorticity is higher near the sides,

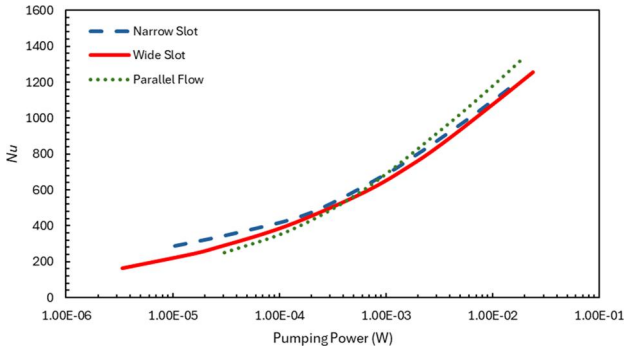

Fig. 8 Variation of Nu with pumping power for different configurations

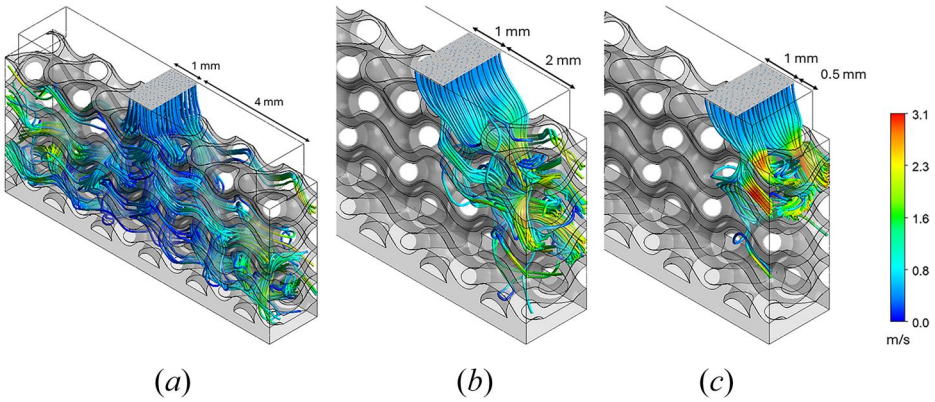

Fig. 9 Streamlines for the wide slot configuration with an inlet velocity of 0.4 m/s

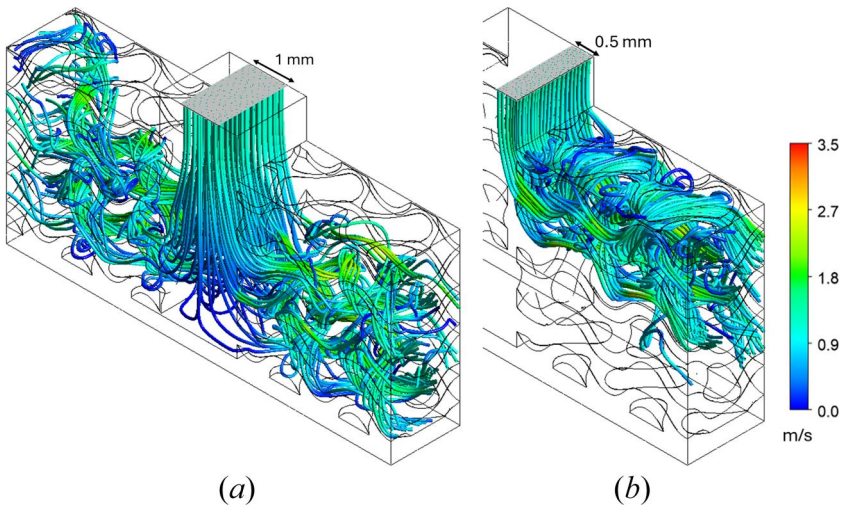

Fig. 10 Streamlines for the narrow slot configuration with an inlet velocity of 1.2 m/s

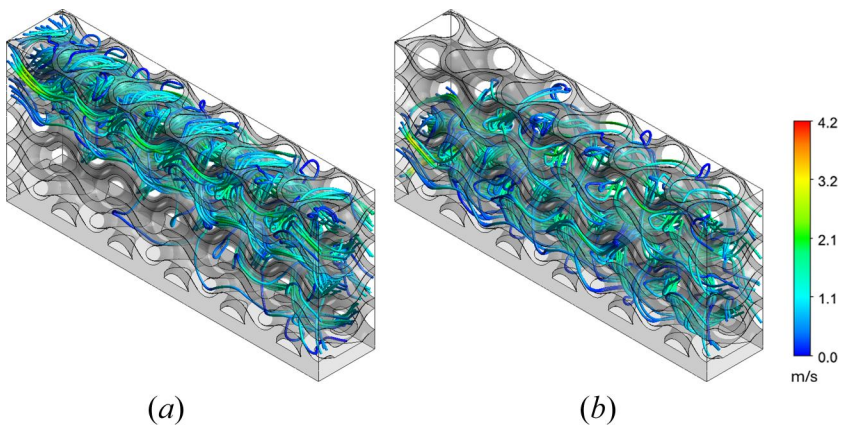

Fig. 11 Streamlines for the parallel flow configuration with an inlet velocity of 0.4 m/s. Streamlines entering the top side (left) and streamlines entering the lower side (right).

especially close to the outlet. Notably, strong vorticity is observed along the surfaces as the flow navigates through curves.

The vorticity results for the narrow slot configuration are shown in Fig. 13. In contrast to the wide slot configuration, vorticity is more homogeneously distributed within the TPMS geometry, indicating more efficient flow mixing. Unlike the wide slot configuration, too high vorticity near the surfaces is not observed when turning through curves. Additionally, the impingement channel in the middle of the geometry does not generate notable vorticity.

The vorticity results for the parallel flow configuration are shown in Fig. 14. Vorticity is present throughout the TPMS geometry from inlet to outlet and is homogeneously distributed. The vorticity patterns in the vertical and horizontal channels resemble those of the narrow slot configuration, resulting in a similar Nu value, as shown

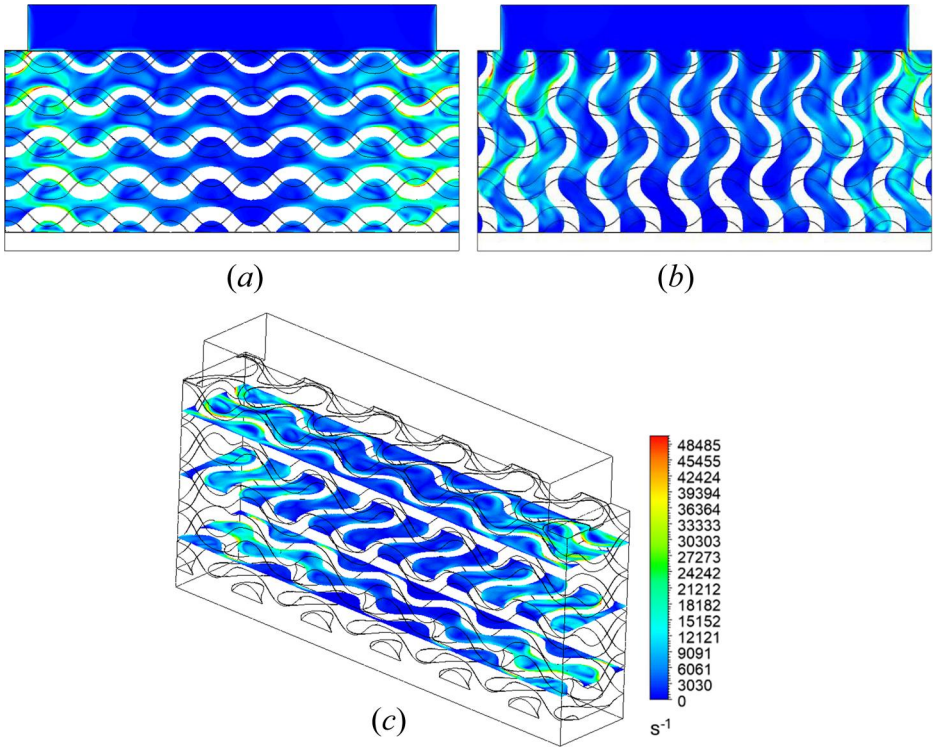

Fig. 12 Vorticity for wide slot configuration with an inlet velocity of 0.4 m/s

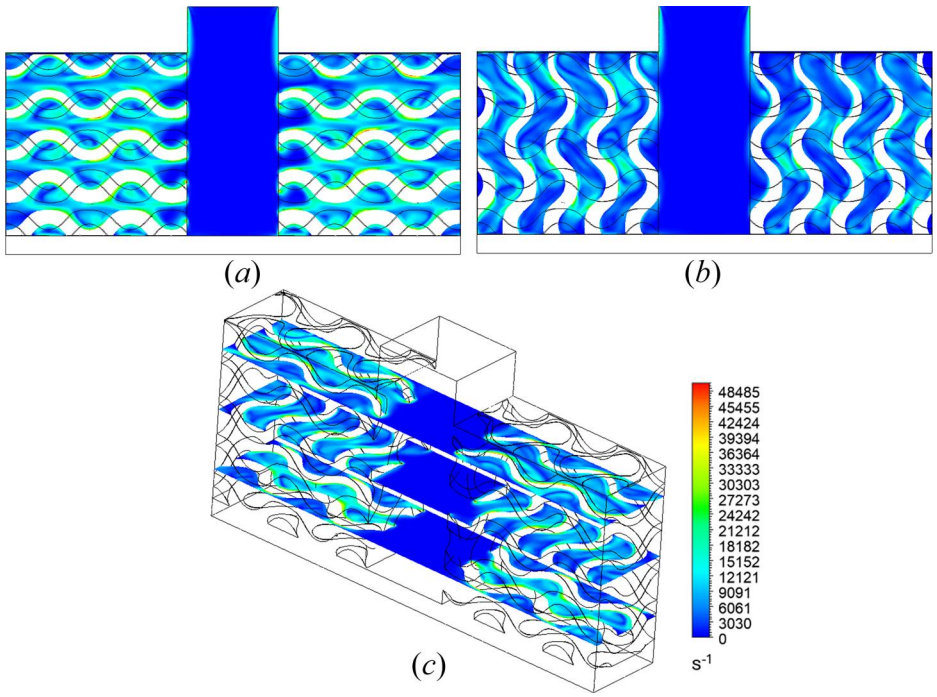

Fig. 13 Vorticity for narrow slot configuration with an inlet velocity of 1.2 m/s

in Fig. 7. However, unlike the narrow slot configuration, high vorticity is observed near the surfaces when the flow turns through curves.

The temperature contours of the solid and fluid regions for the wide slot configuration are shown in Fig. 15. The temperature at the center of the heated surface is slightly higher than at the sides due to the flow being directed toward the outlet before reaching the heated surface. Additionally, the thermal boundary layers are very close to each other in the lower sections, particularly at the center, which is undesirable for efficient heat transfer. This occurs due to the lack of vorticity in these regions, leading to an increased thermal boundary layer thickness.

The temperature distribution in the fluid and solid regions for the narrow slot configuration is shown in Fig. 16. Unexpectedly, the heated surface facing the impingement flow exhibits noticeably higher temperatures due to the lack of heat transfer surface area (e.g.,

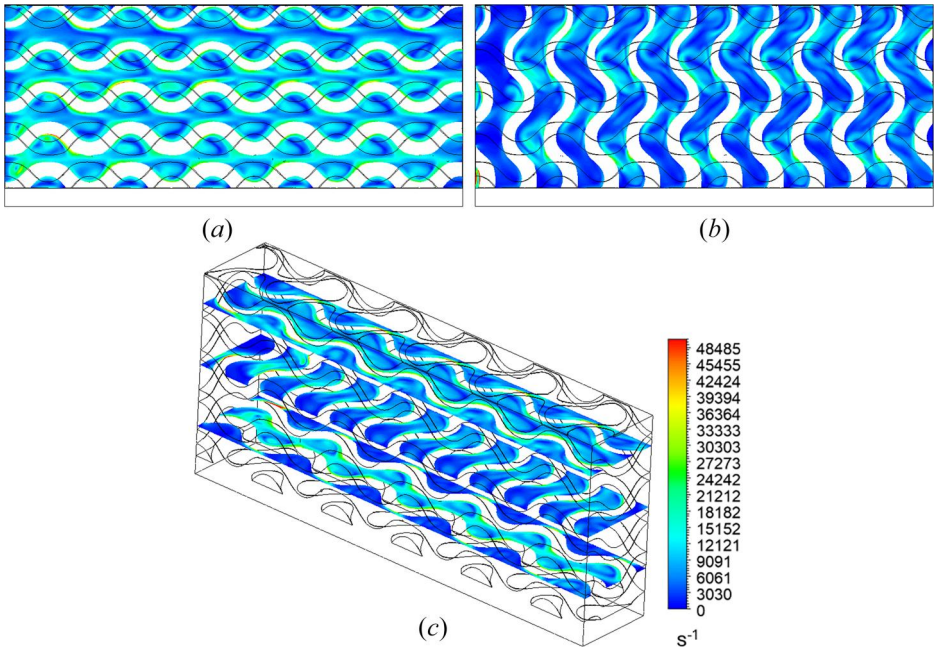

Fig. 14 Vorticity for parallel flow configuration with an inlet velocity of 0.4 m/s

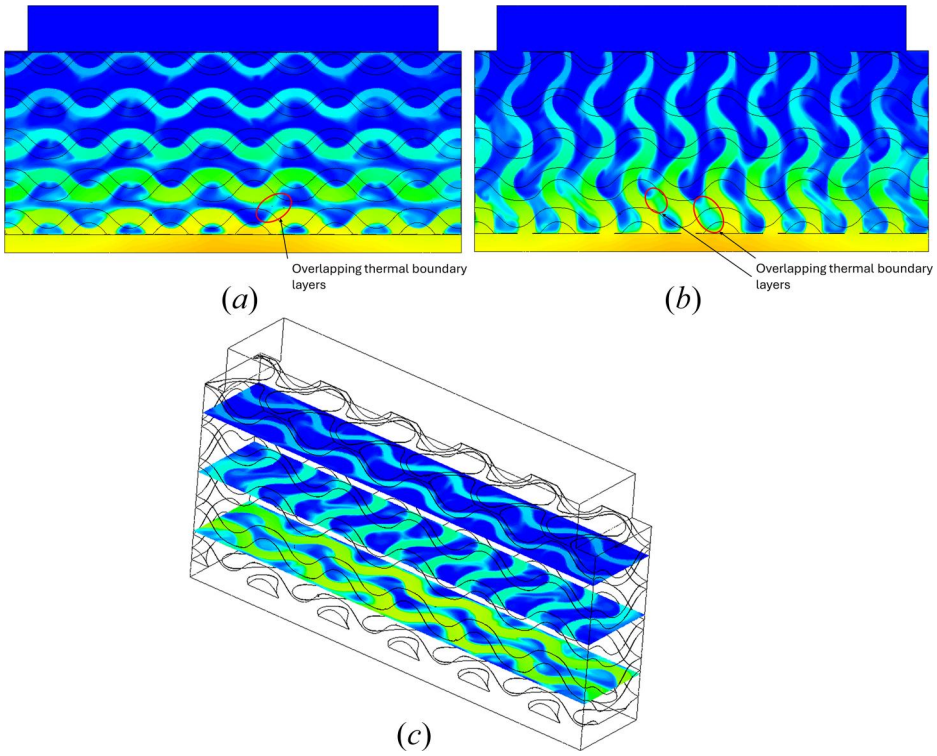

Fig. 15 Temperature contours of solid and fluid for wide slot configuration with an inlet velocity of 0.4 m/s

fins). Given that the heat sources are usually located at the center of the heated surface, this configuration may lead to higher chip temperatures. The thermal boundary layers do not overlap significantly, indicating efficient heat transfer.

The temperature distribution in the solid and fluid regions for the parallel flow configuration is shown in Fig. 17. The temperature of the heated surface increases along the flow as the fluid temperature rises. Additionally, the fluid temperature is higher in the lower sections of the geometry. As the flow progresses, the thermal boundary layers become indistinct, particularly at the lower right section of the geometry, even though the fluid temperature increases significantly.

4 Conclusion

This study investigates the flow and heat transfer characteristics of functional TPMS geometries with different flow configurations. A unit-size TPMS heat sink was modeled with 1.8 mm symmetry

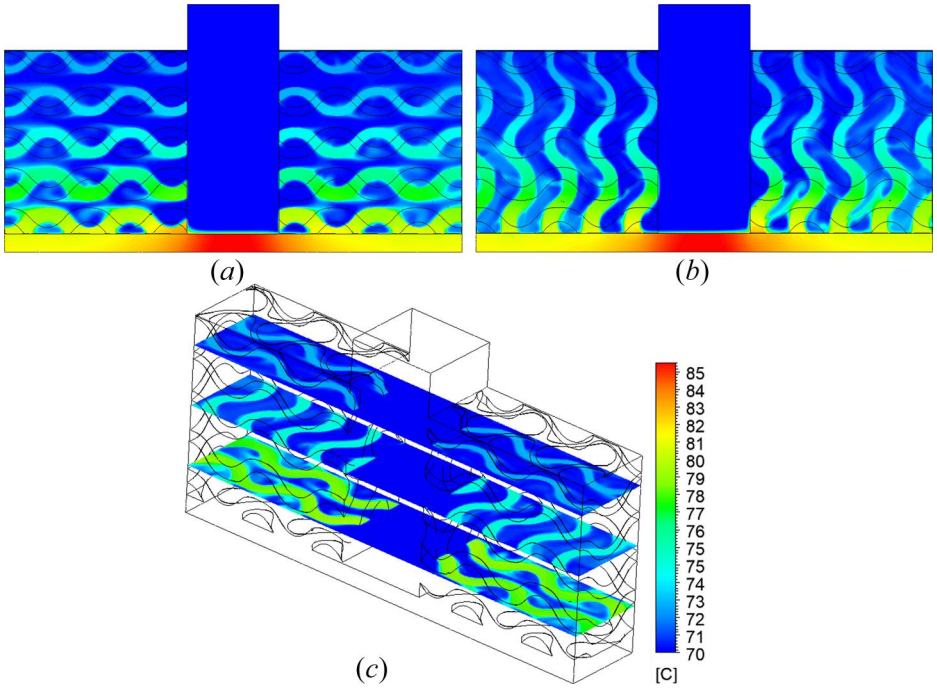

Fig. 16 Temperature distribution in solid and fluid for narrow slot configuration with an inlet velocity of 1.2 m/s

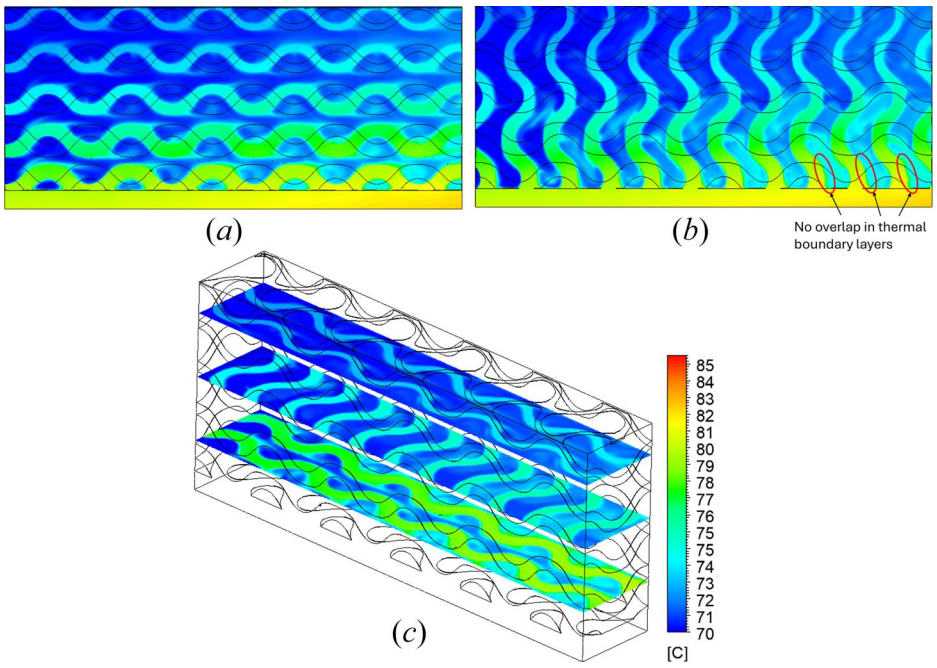

Fig. 17 Temperature distribution in solid and fluid for parallel flow configuration with an inlet velocity of 0.4 m/s

boundaries, a length of 10 mm, and a height of 4 mm. AmpCool® AC-110 dielectric fluid was selected as the coolant, while copper was chosen as the TPMS material. The numerical model was first validated against existing literature. Then, three different flow configurations were analyzed—wide slot, narrow slot, and parallel flow—within a range of 10–1000. The Nu results were presented as functions of Re and pumping power. Additionally, streamlines, vorticity, and temperature distributions were examined.

The parallel flow configuration exhibited higher Nu than the narrow and wide slot configurations. When normalized by pumping power, all three configurations produced similar results, with the parallel flow configuration demonstrating superior performance at higher pumping power levels around 8% and 10% compared to narrow and wide slot configurations, respectively. Moreover, the parallel flow configuration resulted in more uniform heated surface temperatures. The enhanced thermal performance of the parallel flow configuration is primarily attributed to improved flow mixing, as confirmed by vorticity analysis. Unlike impingement-dominated flows, which suffer from limited lateral mixing, the parallel flow promotes distributed vorticity throughout the structure, enabling

more efficient heat transfer. Due to its ease of implementation, the parallel flow configuration was selected for further investigation. The key learnings can be listed as follows:

- Parallel flow TPMS configuration is thermally effective and simpler to implement among the other configurations examined in this study.
- It provides enhanced flow mixing, as evidenced by distributed vorticity throughout the geometry, leading to improved heat transfer performance.
- The functional porosity helps the flow distribute to the upper regions. Therefore, functional porosity can be used to route the flow passively in order to contribute to heat transfer.
- It ensures more uniform temperature profiles, which are crucial for thermal reliability in power electronics applications.

Acknowledgment

The authors thank Susan Rogers and Fernando Salcedo, Technology Development Managers of the Electric Drive Technologies Program under the U.S. Department of Energy Office of Energy Efficiency and Renewable Energy Vehicle Technologies Office.

The Georgia Institute of Technology acknowledges support for this study from the U.S. Department of Energy under award DE-EE0008708. This work was co-authored in part by the National Renewable Energy Laboratory for the U.S. Department of Energy (DOE) under Contract No. DE-AC36-08GO28308. Funding provided by the U.S. Department of Energy Office of Energy Efficiency and Renewable Energy Vehicle Technologies Office. The views expressed in the article do not necessarily represent the views of the DOE or the U.S. Government. The U.S. Government retains and the publisher, by accepting the article for publication, acknowledges that the U.S. Government retains a nonexclusive, paid-up, irrevocable, worldwide license to publish or reproduce the published form of this work, or allow others to do so, for U.S. Government purposes.

Funding Data

- National Renewable Energy Laboratory the U.S. Department of Energy (DOE) (Contract No. DE-AC36-08GO28308; Funder ID: 10.13039/100006134).
- Georgia Tech DOE Office of Energy Efficiency and Renewable Energy Vehicle Technologies Office (Award No. DE-EE0008708).

Data Availability Statement

The datasets generated and supporting the findings of this article are obtainable from the corresponding author upon reasonable request.

References

[1] Elasser, A., and Chow, T. P., 2002, "Silicon Carbide Benefits and Advantages for Power Electronics Circuits and Systems," Proc. IEEE, **90**(6), pp. 969–986.
[2] Seal, S., and Mantooth, H. A., 2017, "High Performance Silicon Carbide Power Packaging—Past Trends, Present Practices, and Future Directions," Energies, **10**(3), p. 341.
[3] Yu, Z., Li, M., and Cao, B., 2024, "A Comprehensive Review on Microchannel Heat Sinks for Electronics Cooling," Int. J. Extreme Manuf., **6**(2), p. 022005.
[4] Chen, H., Ruan, X.-H., Peng, Y.-H., Wang, Y.-L., and Yu, C.-K., 2022, "Application Status and Prospect of Spray Cooling in Electronics and Energy Conversion Industries," Sustainable Energy Technol. Assess., **52**, p. 102181.
[5] Jones-Jackson, S., Rodriguez, R., and Emadi, A., 2021, "Jet Impingement Cooling in Power Electronics for Electrified Automotive Transportation: Current Status and Future Trends," IEEE Trans. Power Electron., **36**(9), pp. 10420–10435.
[6] Zhao, J., Zhang, X., Swaminathan, N., and Haran, K. S., 2022, "An Overview of High Specific Power Electrical Machines and Drives Technologies for Electrified Aircraft," IEEE Energy Conversion Congress and Exposition (ECCE), Detroit, MI, Oct. 9–13, pp. 1–8.
[7] Li, Y., Gong, L., Xu, M., and Joshi, Y., 2021, "A Review of Thermo-Hydraulic Performance of Metal Foam and Its Application as Heat Sinks for Electronics Cooling," ASME J. Electron. Packag., **143**(3), p. 030801.
[8] Tang, W., Zhou, H., Zeng, Y., Yan, M., Jiang, C., Yang, P., Li, Q., et al., 2023, "Analysis on the Convective Heat Transfer Process and Performance Evaluation of Triply Periodic Minimal Surface (TPMS) Based on Diamond, Gyroid and Iwp," Int. J. Heat Mass Transfer, **201**, p. 123642.
[9] Ansari, D., and Duwig, C., 2024, "A Gyroid TPMS Heat Sink for Electronic Cooling," Energy Convers. Manage., **319**, p. 118918.
[10] Wei, F., Sun, X., Lv, Z., Cai, L., Zhai, F., Kong, C., Shi, J., and Zhang, H., 2025, "Optimized Design and Simulation Study of Liquid-Cooled Heat Sink Model for IGBT Module Based on TPMS Structure," ASME J. Therm. Sci. Eng. Appl., **17**(5), p. 051001.
[11] Khalil, M., Ali, M. I. H., Khan, K. A., and Al-Rub, R. A., 2022, "Forced Convection Heat Transfer in Heat Sinks With Topologies Based on Triply Periodic Minimal Surfaces," Case Stud. Therm. Eng., **38**, p. 102313.
[12] Yeranee, K., and Rao, Y., 2022, "A Review of Recent Investigations on Flow and Heat Transfer Enhancement in Cooling Channels Embedded With Triply Periodic Minimal Surfaces (TPMS)," Energies, **15**(23), p. 8994.
[13] Chen, M., Shi, Y., Yang, L., Yan, C., Su, B., Fu, H., Dou, Z., and Chen, Y., 2025, "Performance Evaluation for Additively Manufactured Heat Sinks Based on Gyroid-TPMS," Therm. Sci. Eng. Prog., **60**, p. 103499.
[14] Hajialibabaei, M., and Saghir, M. Z., 2025, "Experimental Study on Heat Transfer Performance of FKS-TPMS Heat Sink Designs and Time Series Prediction," Energies, **18**(13), p. 3459.
[15] Oh, S.-H., Kim, J. E., Jang, C. H., Kim, J., Park, C. Y., and Park, K., 2025, "Multifunctional Gradations of TPMS Architected Heat Exchanger for Enhancements in Flow and Heat Exchange Performances," Sci. Rep., **15**(1), p. 19931.
[16] Bar-Cohen, A., 1993, "Thermal Management of Electronic Components With Dielectric Liquids," JSME Int. J. Ser. B Fluids Therm. Eng., **36**(1), pp. 1–25.
[17] Marto, P., and Lepere, V., 1982, "Pool Boiling Heat Transfer From Enhanced Surfaces to Dielectric Fluids," ASME J. Heat Transfer, **104**(2), pp. 292–299.
[18] Chen, T., and Garimella, S. V., 2007, "Flow Boiling Heat Transfer to a Dielectric Coolant in a Microchannel Heat Sink," IEEE Trans. Compon. Packag. Technol., **30**(1), pp. 24–31.
[19] Kelly, B., Moreno, G., Myers, S., Narumanchi, S., Joshi, Y., and Graham, S., 2021, "Dielectric Fluids for the Direct Forced Convection Cooling of Power Electronics," 20th IEEE Intersociety Conference on Thermal and Thermomechanical Phenomena in Electronic Systems (iTherm), San Diego, CA, June 1–4, pp. 1–6.
[20] Sung, M. K., and Mudawar, I., 2008, "Single-Phase Hybrid Micro-Channel/Micro-Jet Impingement Cooling," Int. J. Heat Mass Transfer, **51**(17–18), pp. 4342–4352.
[21] Muslu, A. M., Smet, V., and Joshi, Y., 2022, "Compact SiC Power Module With Integrated Power Delivery and Cooling," IEEE Trans. Compon., Packag. Manuf. Technol., **12**(12), pp. 1939–1948.
[22] Mendizábal, J. K., Montazeri, M., Huitink, D., and Miljkovic, N., 2022, "Direct Cooling of a Planar Magnetic Converter Using Dielectric Liquid Forced Convection Enabled by Additive Manufacturing," Int. J. Heat Mass Transfer, **191**, p. 122809.
[23] Moreno, G., Narumanchi, S., Tomerlin, J., and Major, J., 2022, "Single-Phase Dielectric Fluid Thermal Management for Power-Dense Automotive Power Electronics," IEEE Trans. Power Electron., **37**(10), pp. 12474–12485.
[24] Muslu, A. M., and Joshi, Y., 2023, "Single Phase Thermal and Hydraulic Performance of a Hybrid Pin Fin and Schoen-G TPMS Architecture Cold Plate for Electronics Thermal Management," International Heat Transfer Conference Digital Library, Cape Town, South Africa, Aug. 14–18, Paper No. IHTC-17-1105.
[25] Al-Ketan, O., Ali, M., Khalil, M., Rowshan, R., Khan, K., and Al-Rub, R. A., 2020, "Forced Convection CFD Analysis of Architected and 3D Printable Heat Sinks Based on Triply Periodic Minimal Surfaces," ASME J. Therm. Sci. Eng. Appl., **13**(2), p. 021010.
[26] White, F. M., and Corfield, I., 2006, *Viscous Fluid Flow*, Vol. 3, McGraw-Hill, New York.
[27] Ansys, 2013, *Ansys Fluent 17.0 Theory Guide*, Ansys, Inc., Canonsburg, PA.
[28] Engineered Fluids, Inc., 2025, "AmpCool Dielectric Coolant Product Page," Engineered Fluids, Inc., Saint Petersburg, FL, accessed May 12, 2025, https://www.engineeredfluids.com/products/ampcool/
[29] Deng, D., Chen, L., Chen, X., and Pi, G., 2019, "Heat Transfer and Pressure Drop of a Periodic Expanded-Constrained Microchannels Heat Sink," Int. J. Heat Mass Transfer, **140**, pp. 678–690.